Research paper

Visible-light-driven photocatalytic inactivation of *Escherichia coli* K-12 over thermal treated natural magnetic sphalerite: Band structure analysis and toxicity evaluation

Dehua Xia[a,b,*], Huadan Liu[a], Zhifeng Jiang[b,c], Tsz Wai Ng[b], Weng Seng Lai[b], Taicheng An[d], Wanjun Wang[d], Po Keung Wong[b,*]

[a] School of Environmental Science and Technology, Sun Yat-sen University, Higher Education Mega Centre, Guangzhou 510275, Guangdong, China
[b] School of Life Sciences, The Chinese University of Hong Kong, Shatin, NT, Hong Kong SAR, China
[c] Institute for Energy Research, Jiangsu University, Zhenjiang, 212013, Jiangsu, China
[d] Institute of Environmental Health and Pollution Control, School of Environmental Science and Engineering, Guangdong University of Technology, Guangzhou 510006, Guangdong, China

ARTICLE INFO

ABSTRACT

The cost-effective natural magnetic sphalerite (NMS) was thermally treated to further enhance its photocatalytic activity for water disinfection. Within 6 h visible light irradiation, the calcined NMS700 exhibited enhanced *Escherichia coli* inactivation with 6 $\log_{10}$ cfu/mL of cell reduction, while the pristine NMS (NMS0) only showed 2.5 $\log_{10}$ cfu/mL of cell reduction. After calcination, the pristine binary composite of ZnS/FeS for NMS0 was transformed into a ternary $ZnS/ZnFe_2O_4/ZnO$ composite for NMS700. The optimum photocatalytic activity of NMS700 was attributed to the efficient charge separation originated from the three-level electron transfer system, well evidenced by the highest photocurrent and fastest electron-hole separation among all the calcined NMS samples. Scavenger study and probe determination demonstrated that the dominant bactericidal agent was changed from superoxide radical ($\cdot O_2^-$) for NMS0 to hole (h^+) and hydroxyl radical ($\cdot OH$) for NMS700. Moreover, vibrating sampling magnetizer (VSM) analysis revealed that the saturated magnetism was enhanced from 0.03 emu/g for NMS0 to 0.15 emu/g for NMS700, due to the appearance of magnetic component like $ZnFe_2O_4$. In addition, NMS0 were not genotoxic but cytotoxic, while NMS700 was toxic of both, indicating the superior stability of NMS700 was obtained after calcination treatment. The study demonstrated that the calcination is an effective strategy to modify natural mineral-photocatalyst into highly effective photocatalyst activated by solar energy.

1. Introduction

During the past decade, harvesting and conversion of solar energy through photocatalysis has a wide range of environmental and energy applications [1,2]. For solar spectrum, ultraviolet (UV) light accounts for only about 5%, while visible light (VL) constitutes about 46% [3]. The widely utilized TiO_2 has a large band gap (3.0 eV for rutile and 3.15 eV for anatase), corresponding to the UV region of the light spectrum, which was only able to utilize a small portion of sunlight spectrum. Therefore, development of visible-light-driven (VLD) photocatalysts capable of utilization of sunlight arouses considerable research interest. Coupling two or more semiconductors is one of the commonly employed techniques for extending the activity of wide band gap photocatalysts into the VL spectrum of sunlight [4,5].

Generally, most composite photocatalysts are often synthesized from expensive chemicals in high purity and may involve complex steps under special conditions [4–6]. Hence, the cost of these synthesized composite photocatalysts in a large quantity can be very high. Recently, naturally occurring minerals such as vanadium bearing rutile, natural sphalerite, and natural pyrrhotite were found to behave like coupled semiconductors, exhibiting good photocatalytic activity under VL irradiation [7–12]. The VLD photocatalytic activities of these minerals were mainly attributed to the substitution of transition metal ions and surface defects. For instance, natural sphalerite can inactivate *E. coli* and degrade methyl orange upon VL irradiation [7–11]. However, the VLD photocatalytic activity of the naturally occurring minerals is relatively low, which need sacrificial agents to enhance its photocatalytic activity such as ascorbic acid [9,10] and hydrogen peroxide [12]. The

addition of sacrificial agents may cause negative effect to the photo-catalytic process, like contamination of the products and high cost of the sacrificial agents, etc. It is thus needed to employ other techniques for improving the photocatalytic activity of the naturally occurring minerals.

Photocatalytic activity of composite photocatalysts is strongly dependent on their chemical composition and surface properties [6,13–15]. Calcination is a good method to alter the composition and properties of photocatalysts, thus to elevate its photocatalytic activity [5,13]. For instance, the calcined natural pyrrhotite at 600 °C (NP600) in air had *E. coli* inactivation rate of nearly 3 times higher than that of untreated natural pyrrhotite (NP), attributed to the formation of Z-scheme (maghemite and pyrite) photocatalysis system in NP600 [16]. In addition, the saturated magnetism of NP after thermal treatment was enhanced with the formation of ferromagnetic maghemite. Motivated by this work, it is promising to calcine other natural mineral photocatalyst, analyze its change in band structure and determine its photocatalytic activity.

Recently, natural magnetic sphalerite (NMS) was proven to be a good mineral photocatalysts, it can totally inactivate 7 $\log_{10}$ cfu/mL *E. coli* within 6 h light irradiation and was capable to recycle with a magnet [18]. Therefore, the aim of the present work was to investigate the effect of calcination temperature for NMS, with a view to improve its VLD photocatalytic activity and magnetic property. The NMS samples were thermally treated and the physiochemical properties of calcined NMS were characterized to better understand its photocatalytic mechanism. Toxicity tests were also conducted to analyze the stability of calcined NMS.

2. Experimental

2.1. Materials

The natural magnetic sphalerite (NMS) sample was obtained from a deposit in China. The NMS sample was crushed into powder and then sieved to obtain fine powder with particle size below 38 μm. Calcination of the NMS powders was conducted in furnace (Vulcan 3-1750, USA) from room temperature to the designated temperature ranging from 500 to 800 °C with a heating rate of 10 °C/min for two hours each. The pristine NMS is abbreviated by NMS0. The calcined NMS samples were abbreviated by NMS500, NMS600, NMS700 and NMS800, corresponding to calcination temperatures of 500, 600, 700 and 800 °C, respectively.

2.2. Characterization

The X-ray diffraction (XRD) spectra of as-prepared NMS products were recorded on the DMAX-2400 diffractor (Rigaku, Japan, Cu Ka = 0.15406 nm) with 40 kV accelerating voltage and 15 mA current. The morphologies of the calcined NMS products were characterized by a scanning electron microscopy (FESEM, FEI, Quanta 400 FEG) equipped with an energy-dispersive X-ray (EDX) spectrometer. UV–vis diffused reflection spectra (DRS) patterns of the calcined NMS products were recorded by a UV–vis spectrophotometer (Lambda 950) with an integral-sphere attachment range from 300 to 800 nm and BaSO$_4$ was used as a reference. The measurement of magnetic properties of the calcined NMS products were conducted by vibrating sample magnetometer (VSM-7300, Quantum design, Lakeshore, USA) at 25 °C.

2.3. Photocatalytic inactivation process

Fifty mL mixture suspension of 1 g/L the calcined NMS products and 10^6 cfu/mL of *E. coli* K-12 in a flask was put into a photocatalytic reactor (Fig. S1) and vigorously stirred by a plastic stirrer. Six fluorescent tubes (FTs) (15 W, VELOX, Thailand) were installed on the side of the reactor as light source, and the VL and UV intensities were determined

by a light meter (LI-COR, Lincoln, Nebraska, USA) and a UVX digital radiometer (UVP, Upland, California, USA), respectively. The light intensity is shown in Table S1. Aliquot samples were collected at different time intervals and diluted serially with sterilized saline (0.9% NaCl) solution, then immediately spread on the Nutrient Agar (Lab M, Lancashire, UK) plate. After that, all the plates were incubated at 37 °C for 24 h to obtain the survival cell numbers. Light control and dark control (without light) were conducted in parallel to study whether photolysis or NMS alone could cause the cell death [17].

2.4. Fluorescence spectroscopy and toxicity evaluation

During the photocatalytic treatment process, 1 mL of solution containing NMS700 and *E. coli* K-12 suspension were collected at several time intervals, concentrated to 0.1 mL by centrifuge and then stained with the dye mixture of LIVE/DEAD BacLight Bacterial Viability Kit (L7012, Molecular Probes, Inc. Eugene, OR) [18]. After being incubated at 25 °C in the dark for 15 min, the prepared samples were pipetted onto a cover-slip and observed by a light microscope (Nikon ECLIPSE 80i, Japan), which was equipped with a filter block NUV-2A consisting of excitation filter Ex 400-680(Nikon, Japan) and Spot-K slider CCD camera (Diagnostic Instruments. Inc. USA).

The acute toxicity towards the photobacterium V. fischeri was measured using a commercial bioassay kit (BioToxTM, Aboatox Oy, Finland) according to the ISO 11348-3 test protocol. After mixing 500 μL of NMS0 or NMS700 solutions with 500 μL luminescent bacterial suspensions, the bioluminescent intensity (BI) after 1 h contact time was measured by a Microtox® Model 500 Analyzer (Azur Environmental) [19]. The obtained data was used to calculate the inhibition rates based on the following equation:

Cell viability (%) = BI$_{treated}$/BI$_{control}$ × 100%

The UMU-ISO 13829 test kit is a convenient approach for the detection of genotoxic activity of chemicals, which utilizes the cell's own repair mechanism for the detection of genotoxicity [20]. The underlying principle of the test is that the DNA damage induces the synthesis of a readily detectable enzyme, which upon contact with a chromogenic substrate develops color formation that is measured spectrophotometrically at 600 nm. In the present study, the genotoxic effects of the NMS0 and NMS700 solutions were determined by calculating the induction ratio (IR) for each sample dilution relative to the respective blank and negative/positive controls in accordance with the test protocol. Several concentrations of the NMS0 and NMS700 solutions were prepared for the test. A test sample is considered to be genotoxic if its IR value is > 1.5.

2.5. Photoelectrochemical measurements

The electrochemical measurements were carried out in a three-electrode quartz cells (an electrochemical workstation, CHI760B). Pt wire was used as the counter electrode and saturated calomel electrodes (SCE) as the reference electrode. The working electrode was obtained according to the following process: 0.1 g of the calcined NMS products were added to nafion/ethanol solution, then spread on the pretreated ITO (0.5 cm × 1 cm), and dried in air to form photocatalysts modified ITO. A 500W Xenon lamp was utilized as the light source in the photoelectrochemical measurements [21].

3. Results and discussion

3.1. Characterization of the pristine and calcined NMS

3.1.1. Phase transformation

The XRD patterns of the pristine and calcined NMS samples are displayed in Fig. 1. NMS0 features prominent peaks at 2θ = 28.5°
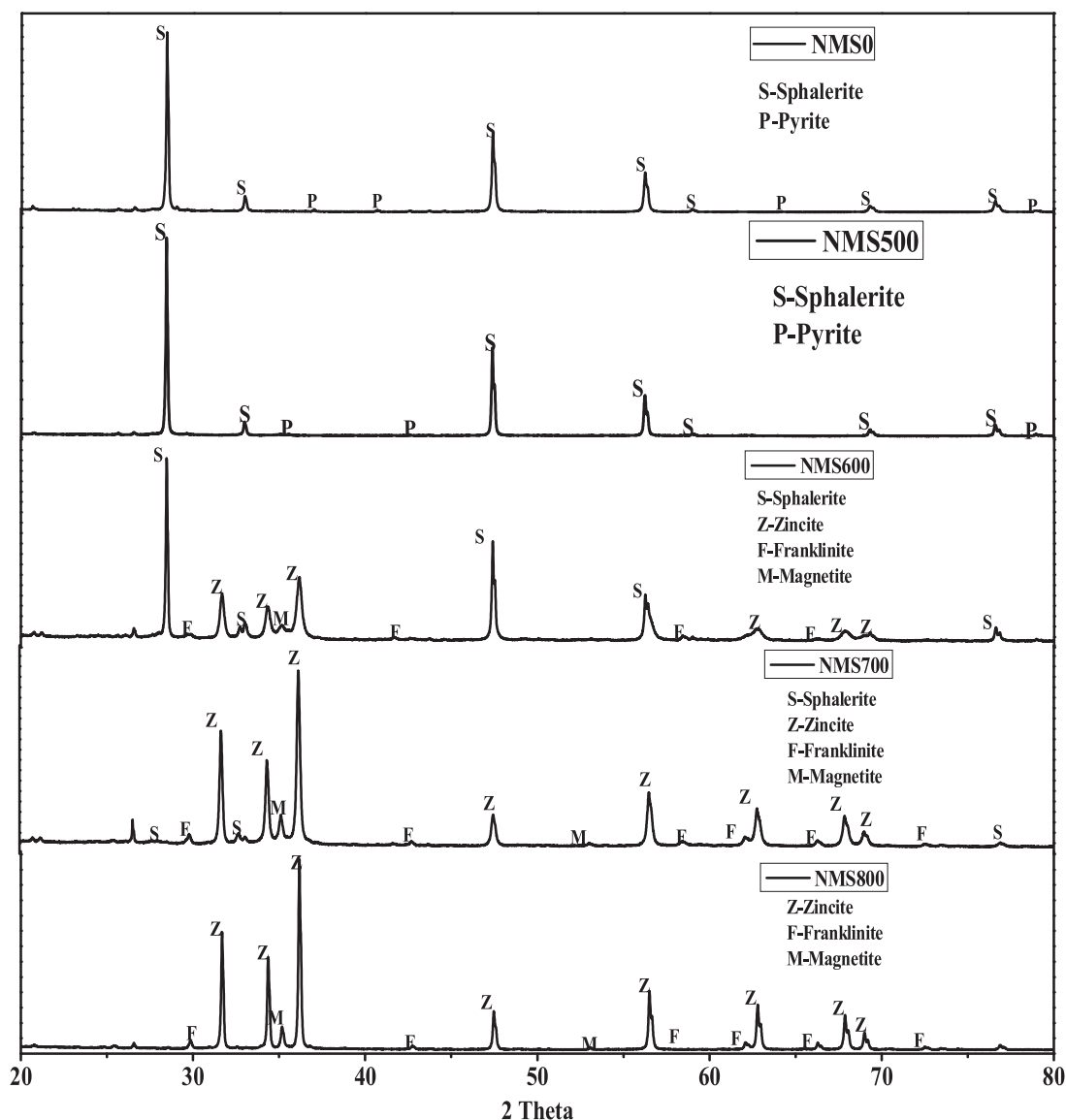
Fig. 1. XRD patterns of NMS0, NMS500, NMS600, NMS700, and NMS800.

(111), 33.1° (200), 47.5° (220), 56.3° (311), 69.4° (400) and 76.6° (331), well indexed to sphalerite (ZnS, JCPDS 77-2100) [22]. Also observed in the XRD spectra are some minor peaks, which could be identified as the presence of iron sulfide like pyrite (FeS$_2$, JCPDS 42-1340) with peaks at 2θ = 37.1° (210), 40.8° (211), 61.7° (023), 64.3° (321) [23]. This can be attributed to the dispersion of some impurities in the sphalerite matrix. Meanwhile, NMS500 also had similar pattern with NMS0, and the peak intensity for each chemical phase has increased, suggesting that the crystallite structure of the NMS0 has been improved after calcination.

In addition to the major characteristic peaks of ZnS, the XRD pattern of NMS600 (Fig. 1) features a new set of peaks at 2θ = 31.8° (100), 34.4° (002), 36.3° (101), 47.5° (102), 56.6° (110), 62.9° (103), 66.4° (200), 67.9° (112), 69.1° (201), corresponding to the standard curve of zincite (ZnO, JCPDS 79-2205) [24]. Hence, NMS600 is mostly composed of crystalline ZnO and ZnS, in which the peaks of ZnO appeared while that of ZnS weakened. The concurrence of both phases proved that 600 °C should be the transition temperature of these two crystalline phases. Meanwhile, the trace peaks of iron compounds in NMS600 were partially changed into franklinite (ZnFe$_2$O$_4$, JCPDS 79-1500) with non-overlapped peaks of 30.0° (220), 35.3° (331), 42.9° (400), 53.2° (422), 62.3° (440), 73.7° (533) and overlapped peaks of magnetite (Fe$_3$O$_4$,

JCPDS 89-0688) with peaks at 43.0° (400) and 66.7° (442) [16,25].

Further increasing the calcined temperature, the XRD pattern of NMS700 is dominated by the peaks of ZnO with traceable ZnS, while NMS800 is devoid of ZnS peaks (Fig. 1). Therefore, the temperature required for the complete conversion of ZnS to ZnO is 700–800 °C for NMS. It has been reported by Zhao et al. [26] that complete conversion of pure ZnS to ZnO occurs at 700 ∘C. Thus, it also indicates the impurities contained in the NMS have some effect on the conversion temperature. Moreover, NMS800 is more crystalline than NMS700 because the peaks of the former are more intense and narrower than those of the latter. Similarly, the trace peaks of ZnFe$_2$O$_4$ and Fe$_3$O$_4$ also become more obvious at higher calcination temperature.

3.1.2. Surface morphology

Fig. 2 showed a significant change in the surface morphology of the NMS after calcination. The surface of NMS0 is characterized by irregularly shaped particles with a wide range of particle size ranging from submicron to over 10 μm. For the EDS analysis, besides the major elements (Zn and S) identified in the XRD analysis, Fe, Al, Si and C were also found. With the calcination temperature increased to 500 °C, the surface of NMS500 has become ruptured and appeared to be attached by submicron clusters of grains. Further increasing the calcination
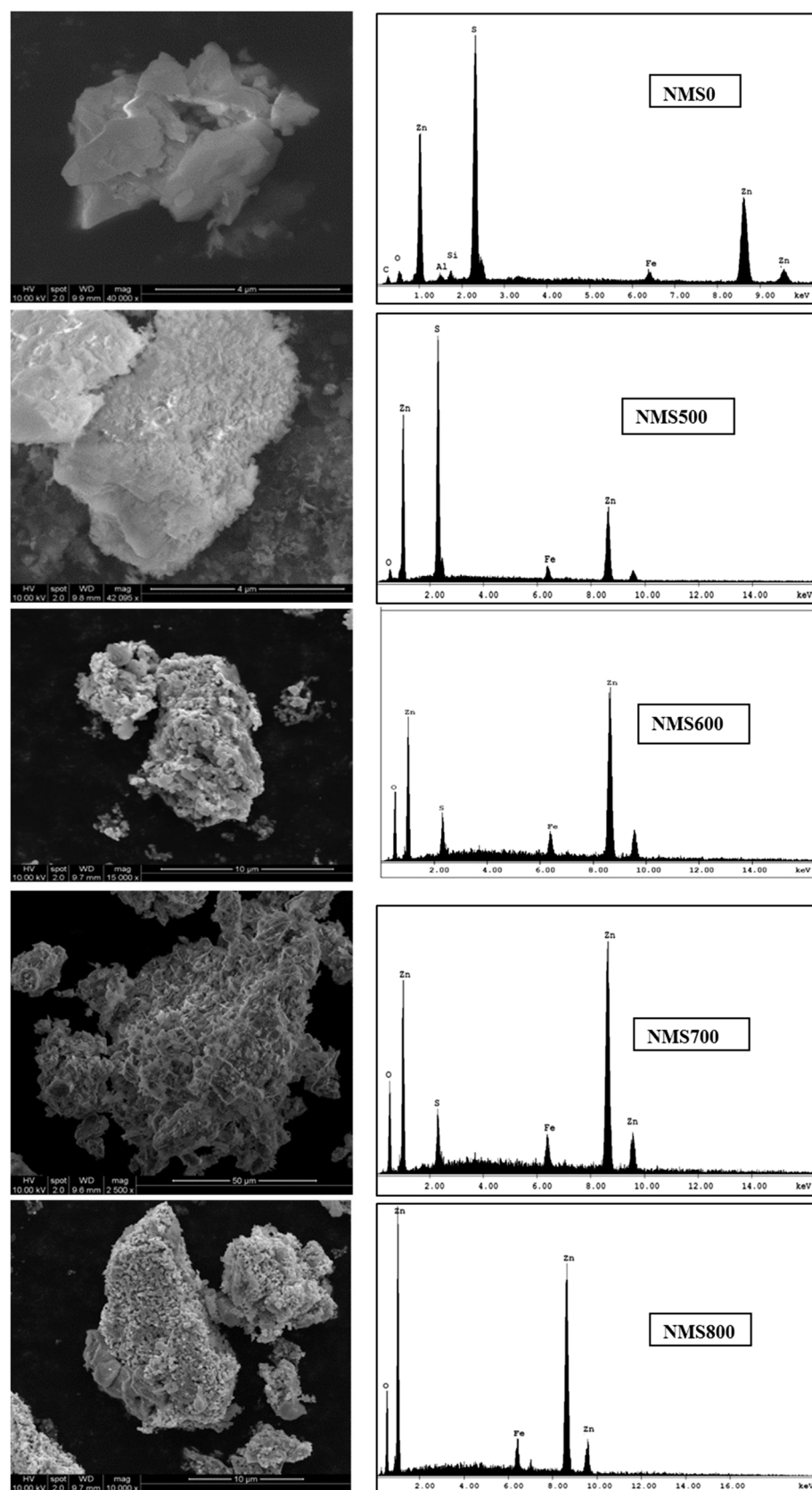
Fig. 2. SEM images and EDX analysis of NMS0, NMS500, NMS600, NMS700, and NMS800.

temperature, these grains became much smaller with some interparticle voids occurred on the surface of NMS700 and NMS800. These voids mainly induced by the release of SO$_2$ during NMS calcination, which are beneficial for enhancing the specific surface area of calcined NMS [5]. In the EDS spectra, it is noteworthy that the sulfur amount in NMS was decreased and totally diminished with the increasing calcination temperature. Meanwhile, the oxygen amount in the calcined NMS was increased, further confirming the phase transformation of ZnS to ZnO.
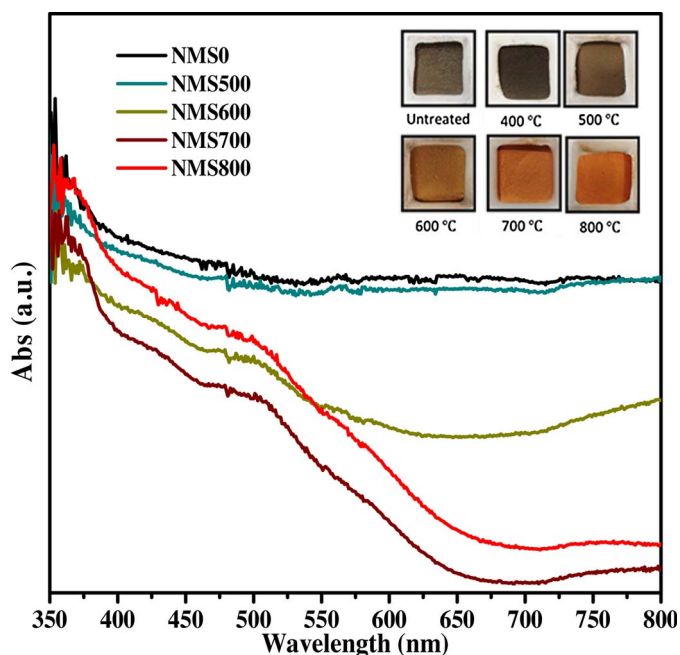
Fig. 3. UV–vis absorption results and photos (inset) of NMS0, NMS500, NMS600, NMS700, and NMS800.

3.1.3. Light adsorption ability

In general, both pure ZnS (3.7 eV) and ZnO (3.4 eV) should have the maximum absorption wavelength in UV region (< 400 nm) [27]. However, the NMS0 in dark brown color exhibited full absorption of visible light (Fig. 3). This is mainly caused by the doped impurities like iron compounds in NMS0. Then, NMS500 exhibited a gradual decline in light absorption, mainly attributed to the better crystalline of ZnS and disappearance of impurities after calcination. As for NMS600, the color was changed into reddish and a blue shift in the light adsorption was observed, mainly attributed to the appearance of ZnO (3.4 eV). Moreover, with the more transformation of ZnS into ZnO, the blue shift was further enhanced for NMS700 and the integral light absorbance of NMS700 evidently decreased by about 50% compared with NMS0. As for NMS800, a little red shift was observed, mainly caused by the more generation of $ZnFe_2O_4$ (1.85 eV), corresponding to the a little extended light adsorption edge [28].

3.1.4. Magnetic property

Hysteresis loops in Fig. 4 indicated how the magnetism change with the formation of new phases after NMS0 was thermally treated. Attributed to the occurrence of different compounds after calcination, the calcined NMS displayed different shapes of the hysteresis curves, indicating different magnetic properties of calcined NMS samples [29]. As shown in Fig. 4, mainly due to the existence of iron compounds (FeS), NMS0 showed a ferromagnetic property with some remanence and coercivity, and a saturation magnetization of approximately 0.03 emu/ g. As for NMS500, the saturated magnetization value slightly increased to 0.045 emu/g, may be attributed to the decomposition of pyrite (FeS) into ferromagnetic pyrrhotite ($Fe_{1-x}S$) [30]. This was consistent with the results for calcined natural pyrrhotite [16], although the XRD pattern cannot differentiate the little formation of $Fe_{1-x}S$ in the present case. Further increasing the calcined temperature, NMS600 displayed a paramagnetic property and the saturated magnetization value of NMS600 rapidly increased to 0.12 emu/g. This is mainly induced by the appearance of ferromagnetic franklinite and magnetite, as proved by the XRD analysis in Fig. 1 [31]. Similarly, the saturated magnetization value of NMS700 and NMS800 were further enhanced to 0.13 and 0.15 emu/g, respectively. Interestingly, it was found that the magnetic property of calcined NMS was changed from ferromagnetic to paramagnetic when calcination temperature increased to 600 °C. In general, the paramagnetic property and enhanced magnetic strength of calcined NMS could further enhance its application potential, as it could be more easily recycled from the treatment medium by a magnet without occurrence of aggregation [32]. As shown in Fig. S2, the used NMS700 can be easily separated and recycled with a magnetic field.

3.2. Photocatalytic inactivation performance

3.2.1. Inactivation kinetics

The viability of *E. coli* during the photocatalytic experiments with NMS0 and calcined NMS samples are shown in Fig. 5a. Obviously, direct photolysis of *E. coli* is negligible. Only slight reductions of cell density in dark with NMS0 and calcined NMS samples were observed, indicating limited toxicity of these samples (Fig. S3). NMS0 can inactivate $2.5\text{-}\log_{10}$ cfu/mL of *E. coli* after 6 h irradiation, indicating its VLD photocatalytic activity. In contrast, *E. coli* could also be photocatalytically inactivated by all the calcined NMS samples. Compared with NMS0, an enhancement of the inactivation efficiency was observed for NMS500 ($3\text{-}\log_{10}$ cfu/mL) and NMS600 ($4\text{-}\log_{10}$ cfu/mL). Specially, NMS700 behaved the best photocatalytic capability on *E. coli* inactivation, that total $6\text{-}\log_{10}$ cfu/mL of cells were inactivated within 6 h. Afterwards, there was a drastic decrement at NMS800 with *E. coli* loss of only $2.4\text{-}\log_{10}$ cfu/mL. The results indicate the calcination could efficiently enhance the photocatalytic activity of NMS.

Moreover, the processed bacterial membrane integrity in the presence of NMS700 was visually observed through fluorescence microscopy. Although NMS700 can be stained in red, which still can be clearly differentiate from its larger size (about 10 μM) than that of *E. coli* cells (1–2 μM) (Fig. S3). As shown in Fig. 6a–c, after staining with a fluorescent dye mixture, the red fluorescent cells increased in number to replace the green fluorescent cells after prolonged treatment, indicating cell membrane rupture during photocatalytic process [33]. Similarly, SEM images of *E. coli* also indicate ruptures and holes were formed on the surface of *E. coli* cells with prolonged treatment (Fig. 6d–f). This point to the fact that sustainably generated RSs can cause a myriad of adverse effects on the cell envelope.

3.2.2. Variation of primary reactive species

As proposed by previous studies, the band position could alter the generated reactive species, due to the structural and chemical changes after calcination [5,16]. For the NMS0, the scavenger test has observed great inhibition in photocatalytic inactivation efficiency after addition of Fe(II)-EDTA, indicating the major reactive species used to inactivate *E. coli* is H_2O_2 (Fig. 7a). On the other hand, the NMS700 had comparable reduction curve in the presence of oxalate and isopropanol, suggesting the h^+ and ·OH play the major bactericidal role (Fig. 7b). Obviously, there was a shift of major reactive species between the NMS0 and NMS700.

Moreover, the generated reactive oxygen species were directly determined by photometric assays [34]. First, the coumarin could react with H_2O_2 to form highly fluorescent 7-hydroxycoumarin with a maximum intensity at 456 nm (Fig. 8a). Unexpectedly, no H_2O_2 was detected in the presence of NMS0, although it plays the leading role in NMS0. One possible reason the generated H_2O_2 was below the detection limit of this assay due to the low photocatalytic activity of NMS0. In contrast, the generated H_2O_2 was accumulated to 4 μM in the photocatalysis of NMS700. Second, the TA could combine with ·OH to generate 2-hydroxyterephthalic acid, which has the highest emission at 425 nm. Elevated signal was recorded during the photocatalysis by NMS700 rather than NMS0 (Fig. 8b). The results further confirmed the generation and transformation of reactive species in the NMS700.

3.2.3. Photoluminescence spectra and photoelectrochemical analysis

To further analyze the enhanced photocatalytic activity of NMS700, the well-known photoluminescence (PL) emission was utilized to
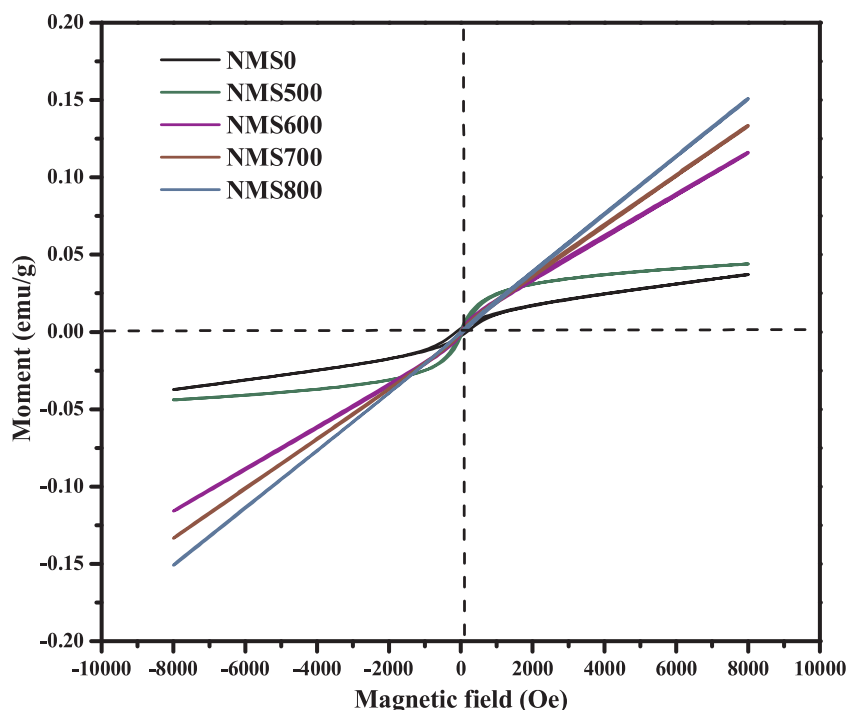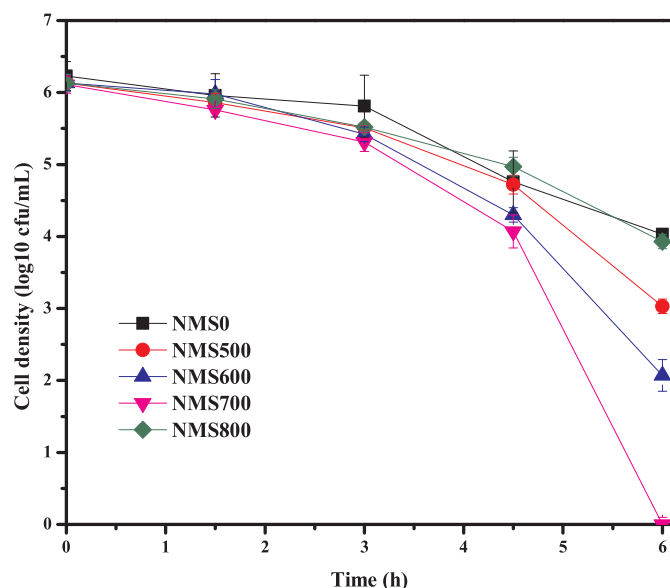
Fig. 5. Photocatalytic inactivation efficiencies of *E. coli* K-12 by NMS0 and NMS calcined at different temperature.

disclose the fate of electron-hole pairs in NMS700. In general, the higher intensity corresponds to the faster recombination. Fig. 9a shows the PL spectra of pristine and calcined NMS excited in 360 nm. The main emission peak of NMS is centered at 495 nm, which can be contributed to the band-band PL phenomenon with the energy of light approximately equal to the band energy of ZnS [35]. The results show that the PL intensity of NMS700 drastically decreased compared with NMS0. These results suggest that the heterostructure among ZnS, $ZnFe_2O_4$, ZnO in NMS700 can effectively diminish the electron-hole recombination rate, as the binary composite of ZnS/FeS in NMS0 was transformed into the tertiary system ($ZnS/ZnFe_2O_4/ZnO$) in NMS700. The PL intensity has strong effect on the photocatalytic activity of the corresponding photocatalysts.

Similarly, in order to further confirm the enhanced ability of

generation, separation and migration efficiency of photogenerated carriers in NMS700, photoelectrochemical measurements were performed. Fig. 9b shows the typical I–t curves for as-prepared electrodes of pristine and calcined NMS with several on-off cycles of intermittent light irradiation at a constant bias of 0.1 V vs. SCE with the measured solution pH of 7.4. The photocurrent increases sharply when the light is switched on, and immediately returns to its initial state after the light source is turned off. The transient photocurrent density of NMS700 is 1.05 times higher than that of NMS0, which demonstrates more efficient charge separation and transportation. Inset of Fig. 9b also gives the photogenerated current ($I_{photo} - I_{dark}$) of pristine and calcined NMS, where I_{photo} and I_{dark} represent the currents in the presence and absence of light irradiation, respectively. It is also found that the transient photocurrent response of NMS700 ternary composite is the highest among the calcined NMS samples, owning to the junction-promoted efficient three-level electron charge separation and improved light absorption.

The surface photovoltage (SPV) spectra responses are direct and reliable means to investigate the nature of photogenerated charges in solid-state semiconductors. The intensity of the SPV signal also reflects the separation of the photogenerated electron-hole pairs. In general, the stronger is the SPV response, the higher is the photogenerated charge separation. Fig. 9c presents the SPV spectra of pristine and calcined NMS. It is clear that the NMS0 has limited SPV signal, while it is apparent that the SPV response of calcined NMS is significantly enhanced, indicating the enhanced charge separation for calcined NMS. In addition, the NMS700 sample with $ZnS/ZnFe_2O_4/ZnO$ hybrid shows the strongest response, which further proves that calcination is favorable for the charge separation enhancement. The results of SPV spectra and photocatalytic inactivation performance illustrate that the band alignment and tight interface present between $ZnS/ZnFe_2O_4/ZnO$ plays an important role in charge carriers separation, which promote the transition of electrons in NMS700, and in turns enhance its photocatalytic activity.

To further examine the effect of calcination on the recombination and kinetics of NMS0 and NMS700, the transient open-circuit voltage (VOC) decay was recorded as a function of time under on-off switching of visible light irradiation (Fig. 9d). The photovoltage decay for the NMS700 has slower than that of the NMS0, confirming a longer electron
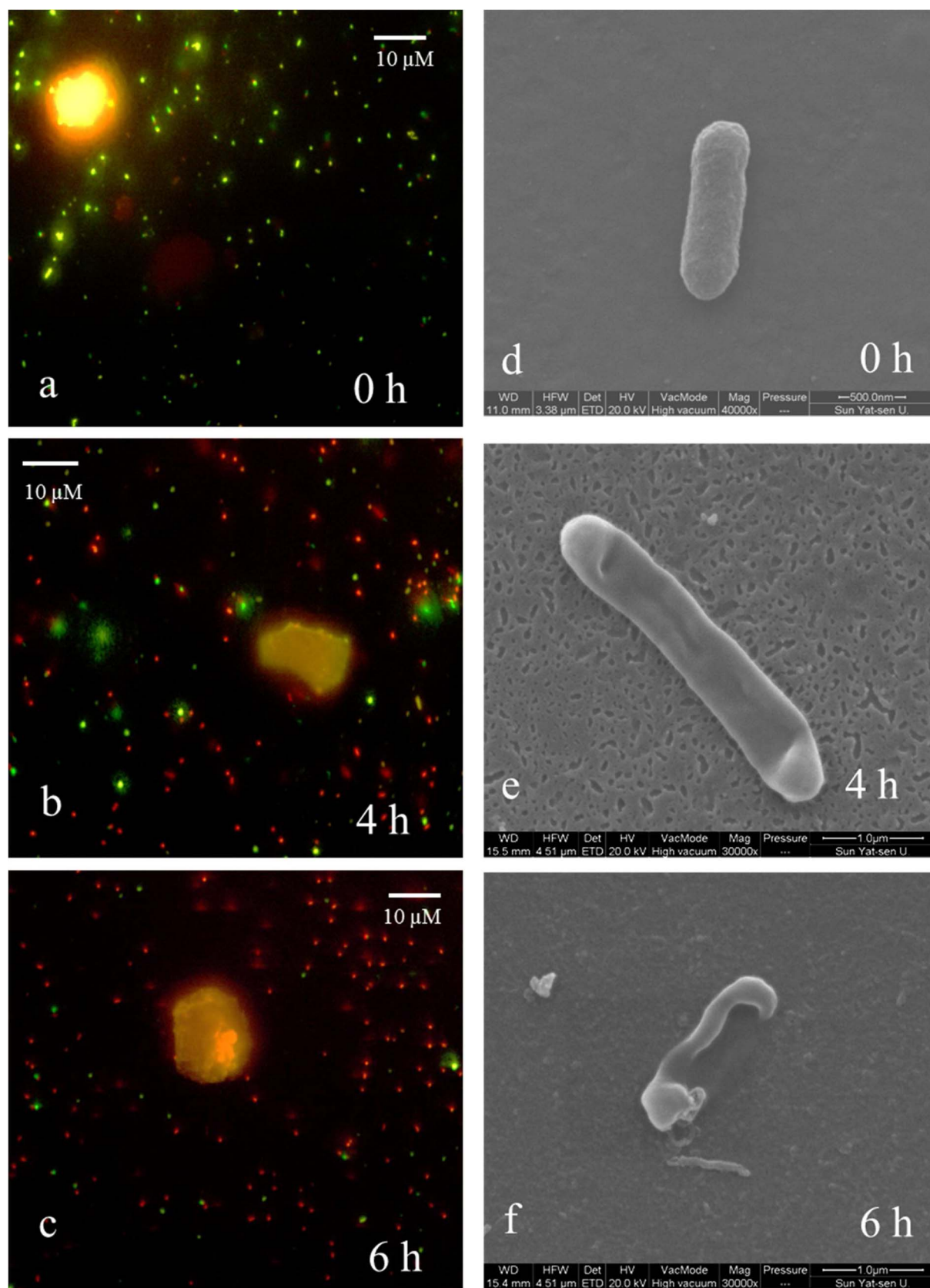
Fig. 6. Fluorescence change of *E. coli* K-12 with NMS700 under light irradiation.
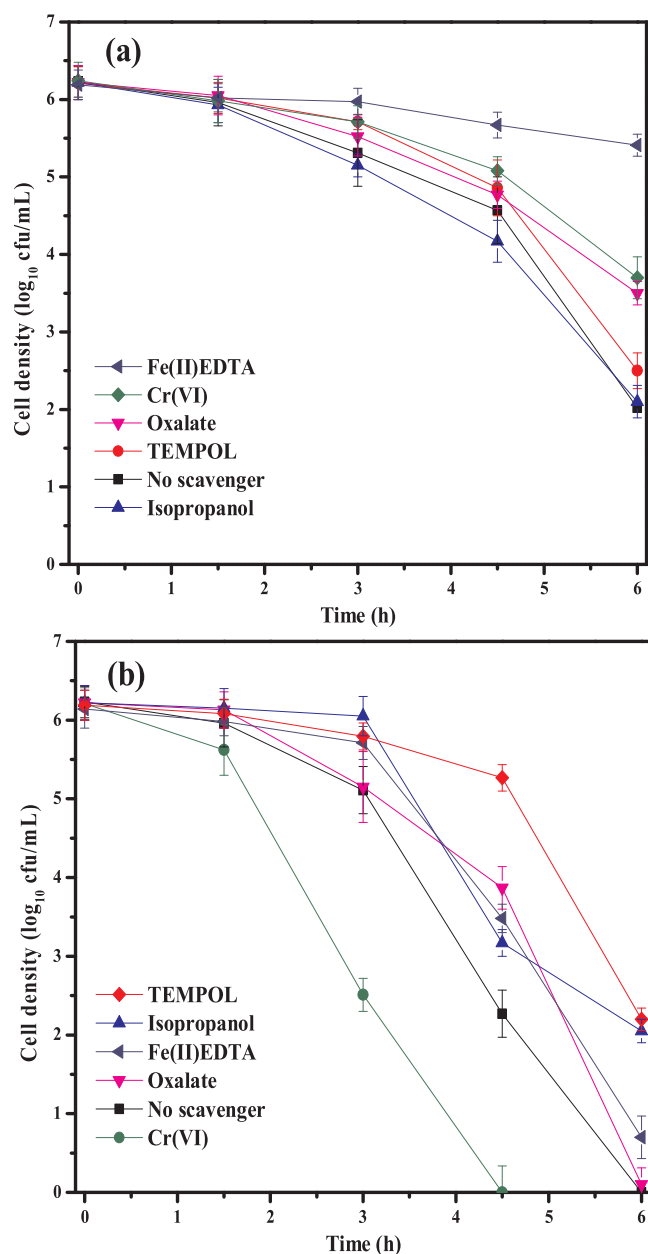
Fig. 7. Photocatalytic inactivation efficiency against *E. coli* K-12 (10^6 cfu/mL, 50 mL) by 1 g/L of NMS0 (a) and NMS700 (b) with addition of different scavengers (0.05 mM Cr (VI), 0.1 mM Fe(II), 2.5 mM isopropanol, 0.5 mM oxalate and 2 mM TEMPOL), respectively.

Fig. 8. (a) Fluorescent intensity of terephthalic acid with generated ·OH and (b) concentration of accumulated H_2O_2 generated by NMS0 and calcined NMS.

lifetime leading to slower recombination kinetics. The longer lifetime of photoelectrons facilitates the availability of a large number of carriers for photocatalytic inactivation. Thus, it is proved by the above photophysical properties that the charge separation of NMS700 is enhanced, which contributed to the excellent photocatalytic performance of NMS700 compared with that of the other calcined samples.

3.2.4. Possible mechanism of elevated activity for calcined NMS

To further reveal the mechanistic pathway occurring at the photocatalyst surface, the band energy alignments were investigated from the Mott-Schottky plots (Fig. 10a). Both NMS0 and NMS700 samples display n-type semiconductor characteristics. As shown in Fig. 10a, the measured CB band of ZnS is at −1.04 V and FeS is at −0.68 V for the ZnS/FeS composite in pristine NMS0, respectively. Therefore, the electrons from ZnS with a higher Fermi level were suggested to migrate toward the lower Fermi level of FeS until the Fermi levels come into
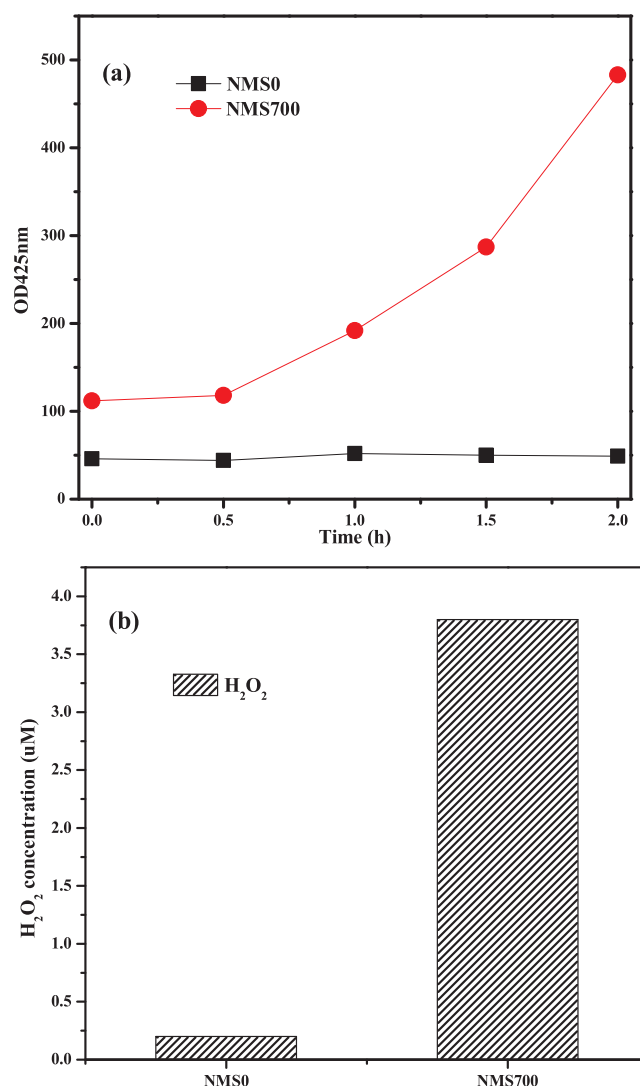
symmetry like Fig. 10b. The *n*-n junction region leads to a potential visible light response at the interfaces of ZnS/FeS. As for NMS700, the flat-band potential (equal to CB band in *n*-type semiconductor) was measured at −1.04 V for ZnS part in ZnS/ZnFe$_2$O$_4$/ZnO composite of NMS700 (Fig. 10a). The second linear region is attributed to the CB band of the ZnFe$_2$O$_4$ part, corresponding to a potential of −0.68 V for the ZnFe$_2$O$_4$ part in the ZnS/ZnFe$_2$O$_4$/ZnO composite of NMS700. Similarly, the measured CB band for the ZnO part is at −0.5 V in NMS700. Obviously, the Fermi level of ZnS is higher than that of ZnFe$_2$O$_4$ and ZnO. When a contact is formed between the three semiconductors in NMS700, the electrons from ZnS with a higher Fermi level will migrate toward the lower Fermi level of ZnFe$_2$O$_4$ and then ZnO until the Fermi levels come into symmetry, as shown in Fig. 10c. After equilibrium is attained between the Fermi levels of the three semiconductors, the internal electric field in the n-n-n junction region leads to a potential difference at the interfaces of ZnS/ZnFe$_2$O$_4$/ZnO, with its field direction from ZnS to ZnFe$_2$O$_4$ and ZnO.

Obviously, the results suggested that the changes in the photocatalytic performances were closely related to the structural modifications of NMS after calcination. As shown in Fig. 5a, the NMS500 displayed a higher performance than NMS0. This is mainly due to the defects diminished on the surface of NMS after calcination, corresponding to the better crystalline phase obtained for NMS500. According to XRD results, NMS0 and NMS500 possess the same hybrid
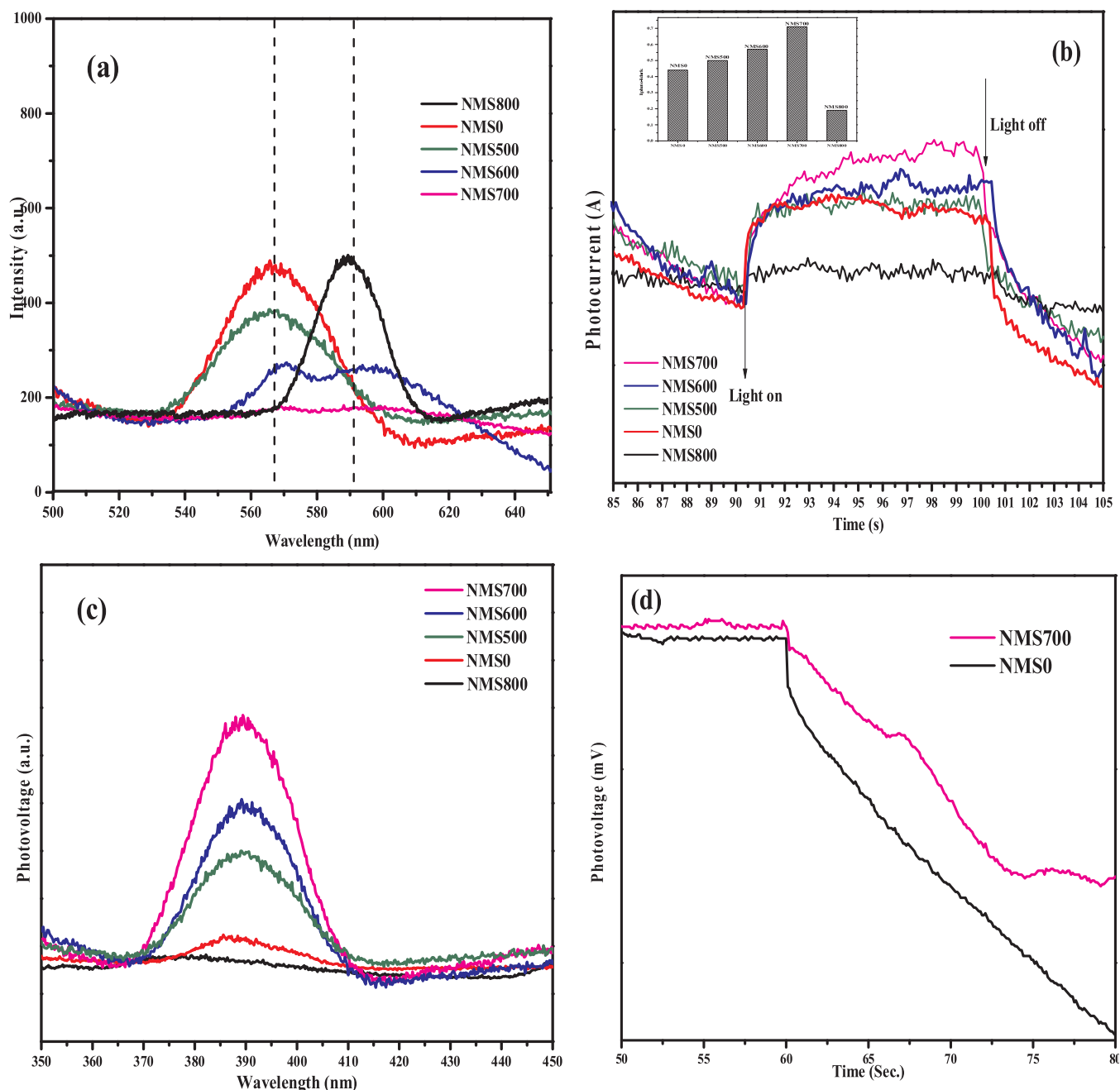
Fig. 9. (a) Photoluminence spectra (b) Time-based photocurrent response and Photogenerated current ($I_{photo} - I_{dark}$) of NMS0 and calcined NMS (inset); (c) The surface photovoltage (SPV) spectra responses of pristine and calcined NMS, (d) Open-circuit voltage decay recorded for NMS0 and NMS700 electrolyte.

composite of ZnS/FeS. Under light irradiation (Fig. 10b), the photo-generated electron on the CB of ZnS (−1.04 V) [22] could transfer to the CB of FeS (−0.53 V) [16], which accelerate the separation of $e^- - h^+$ pairs in ZnS, thereby NMS0 and NMS500 displayed VLD photocatalytic activity. Theoretically, the electron generated from hybrid composite of ZnS/FeS (−0.53 V) in NMS0 is negative enough to reduce the O_2 into H_2O_2 (−0.42 V) [36], thereby the primary bactericidal role of H_2O_2 for NMS0 in scavenger study (Fig. 7a).

As for NMS600, ZnS has been partially transformed into ZnO, thus form into hybrid structure of ZnS/ZnO. Since ZnO (3.4 eV) has smaller band gap than ZnS (3.7 eV) [37], this may allow an easier excitation of the NMS600. Also, little trace amounts of franklinite ($ZnFe_2O_4$) were observed in NMS600. $ZnFe_2O_4$ was reported to achieve a good photocatalytic activity under visible light, due to its narrow band gap of 1.90 eV. Therefore, the present NMS600 may form a ternary composite

of ZnS/ZnFe$_2$O$_4$/ZnO, which is beneficial for the acceleration of $e^- - h^+$ pairs separation. Based on these band structures, the pathway for electron transfer for NMS600 was proposed like Fig. 10c. Accordingly to the Mott-Schottky plots and previous reports [22,36,37], the CB and VB positions of the ZnS and ZnO are ∼ −1.04 V/ + 2.56 V and −0.5 V/ + 2.7 V, while those of the ZnFe$_2$O$_4$ are ∼ −0.68 V/ + 1.17 V, respectively. When the visible light is irradiated on the surface of the NMS600, the photo-generated electrons in the CB of ZnS (−1.04 V) tends to transfer to the CB of ZnFe$_2$O$_4$ (−0.68 V), then further move to the CB of ZnO (−0.5 V). Through this process, the photo-induced carriers within this ternary system can be successfully separated, thus excellent photocatalytic activity can be achieved.

Hence, NMS700 has similar structure of ZnS/ZnFe$_2$O$_4$/ZnO like NMS600 (Fig. 10c), with a long-distance electron transport of the three-level electron transfer system, also achieved an enhanced
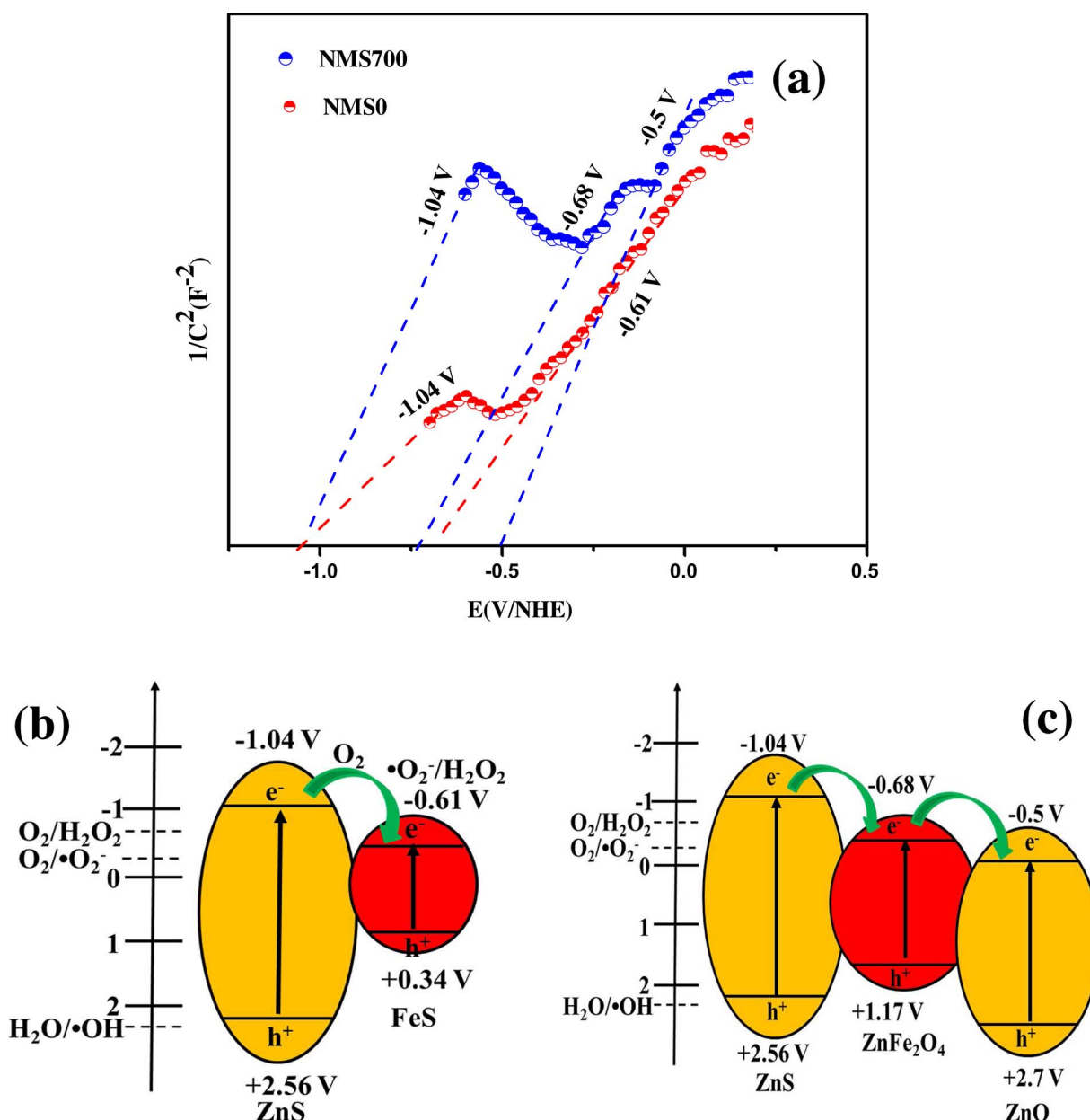
Fig. 10. (a) Mott-Schottky plot of NMS0 and NMS700; proposed mechanism for the visible-light photocatalytic *E. coli* inactivation of the binary composite (ZnS/FeS) in NMS0 (b) and ternary composite (ZnS/ZnFe$_2$O$_4$/ZnO) in NMS700 (c).

photocatalytic performance than NMS0. Especially, ZnO replaced ZnS and became dominant in NMS700, based on the XRD pattern in Fig. 1. NMS700 may obtain an optimum ratio of ZnS/ZnFe$_2$O$_4$/ZnO, and thus even induce a better photocatalytic performance than NMS600. It is proved by the above photo-physical properties that the charge separation of NMS700 is enhanced, corresponding to the strongest photocurrent intensity of NMS700, as well as the SPV and PL results (Fig. 9). The enhanced charge separation can efficiently enhance the generation of crucial photochemical radical product like ·OH, well consistent with the enhanced intensity of fluorescence spectra related to the produced ·OH amount (Fig. 8a). Therefore, in the three-level electron transfer system of NMS700, more h$^+$ was survived on the ZnS because electron was greatly transferred to ZnFe$_2$O$_4$ and ZnO. The h$^+$ with +2.56 V is plausible to oxidize more OH$^-$/H$_2$O into ·OH (E$_0$ = (OH$^-$/·OH) = 2.38 V), thereby the primary bactericidal role of h$^+$ and ·OH for NMS700 in the scavenger study (Fig. 7b). Moreover, there are many voids observed on the surface of NMS700, indicating an increased surface area of NMS, which could also enhance the phtocatalytic

reaction between reactive species and targeted bacterial cells. Hence, these effects may also imply the increasing trend in photocatalytic inactivation efficiency of NMS700.

As for NMS800, the hybrid structure has changed into ZnO/ZnFe$_2$O$_4$. Theoretically, the photogenerated electron on the CB of ZnFe$_2$O$_4$ (−0.37 V) could transfer to the CB of ZnO (−0.31 V), which may accelerate the separation of e$^-$ and h$^+$ in ZnFe$_2$O$_4$. However, the sintering effect happened at 800 °C in the calcined NMS samples, as shown in Fig. 2e. Some studies proposed that such sintering would result in larger grain size and hence smaller specific area of the photocatalyst [16,38]. These may result in drastic reduction of inactivation performance of NMS800. Coincidently, the light absorption is reduced as the sintering effect prevents the visible light absorption from reaching the NMS800 surface, which leads to a great decrease of the photocurrent, SPV signal in comparison to that of the NMS700 sample (Fig. 9).
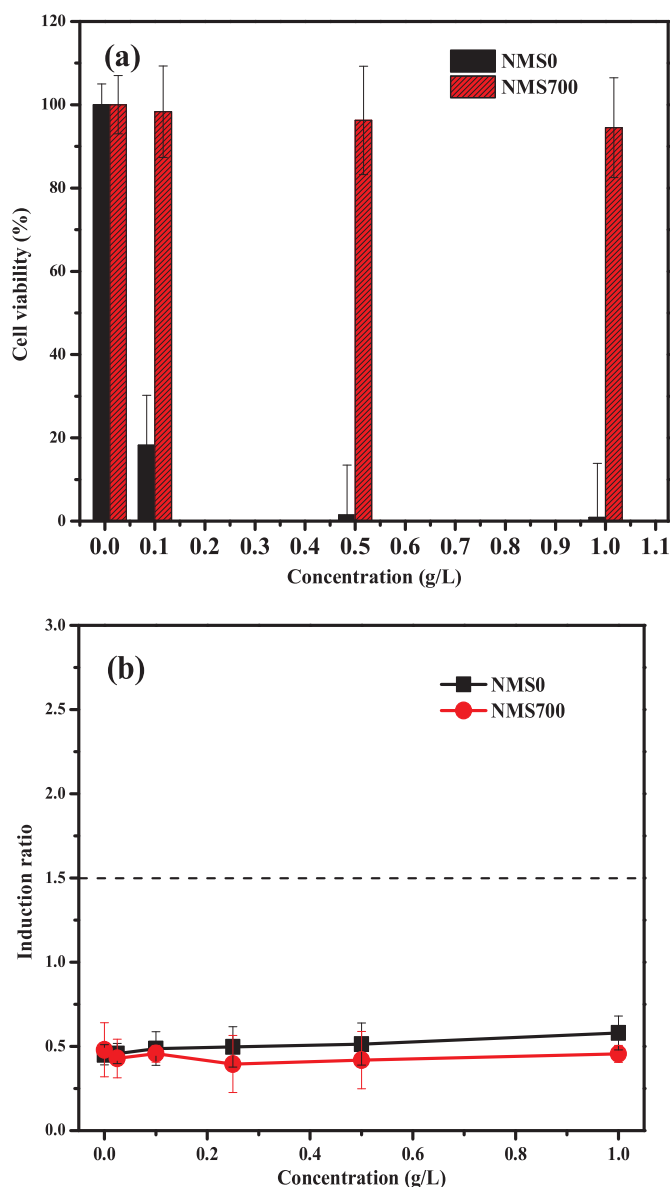
Fig. 11. (a) Changes in percent relative inhibition towards *V. fischeri* after mix with NMS0 and NMS700 at different concentrations; (b) Induction ratios (IR values) determined after mix with NMS0 and NMS700 at different concentrations.

3.3. Toxicity assessment

3.3.1. Acute toxicity

For the potential application in the environment cleanup, the possible cytotoxicity of NMS0 and NMS700 was examined through the Microtox® test with *Vibrio fischeri*, on the basis of the relative photoluminescence and growth inhibition rates towards this marine bacterium [39]. Cells were exposed to concentrations of 0.01, 0.1, 0.5, and 1 g/mL of dispersed sample solutions. Fig. 11a shows the toxic response as percent relative inhibition being recorded after incubation. Obviously, NMS0 was more lethal to cells than NMS700. For NMS0, the cell inhibition effects exhibited a concentration-dependent manner. NMS0 stimulated the cells' loss at a very low concentration of 0.1 g/mL, and aggravated with the enhancement of NMS0 concentration. This is probably due to the leakage of relatively toxic metal ions from NMS0, as the corrosion of Zn^{2+} always happen from metal sulfides [22]. In contrast, the inhibition rate of cells treated by different concentrations of NMS700 always keeps the relatively high value (over 90%), even at the concentration of 1 g/L, revealing the good biocompatibility and low

cytotoxicity of NMS700 for *V. fischeri* cells. This is because calcination could efficiently remove the toxic impurities, proved by the higher crystalline of NMS700 in XRD patterns (Fig. 1). Therefore, the secondary metallic pollution can be efficiently eliminated by calcination for the utilization of natural mineral.

3.3.2. Genotoxicity

Besides the acute toxicology, the leaked metals may also induce mutagenicity, due to their ability to induce mutations and cancerous transformation of normal cells [40]. Therefore, the genotoxicology for NMS0 and NMS700 were evaluated by UMU-ISO test, which is widely used to determine the mutagenic potential of new chemicals [41]. Besides, the test protocol enables the calculation the *Umu induction ratio* I_R after 60 min incubation, an appropriate indicator of a genotoxic response [42]. Fig. 11b depicts the relative enzyme activities (Us values) for NMS0 and NMS700 solution at varying concentrations (0.025, 0.1, 0.25, 0.5 and 1 g/L). Both the same trends were observed for both NMS0 and NMS700, with IR values fluctuate at about 0.5. According to the test protocol, the IR values must be > 1.5 to consider a test sample to be genotoxic, which is not the case for NMS0 and NMS700 samples examined in this work. Especially, the IR value was a little increased when NMS0 at 1 g/L, indicating the cytotoxic but non-genotoxic of NMS0. The genotoxicity results also supported the calcination treatment helped to increase good stability of NMS0.

3.4. Conclusions

Calcination has modified the composition and enhanced the photocatalytic activity of NMS. The optimal sample is NMS700, which can inactivate 6 log_{10} of *Escherichia coli* K-12 within 6 h light irradiation. The improved photocatalytic activity of NMS700 was attributed to the matched energy level position among ZnS, $ZnFe_2O_4$ and ZnO after calcination. Due to the three-level electron transfer system, the major reactive species for *E. coli* inactivation have shifted from H_2O_2 for NMS0 to h^+ and ·OH for NMS700. Calcination has also enhanced the magnetic strength of the NMS. Moreover, NMS0 exhibited an acute toxicity but non-genotoxic, while NMS700 is non-toxic for both tests. This work can provide a facile yet efficient way to modify natural semiconductor into a three-level electron transfer system for environmental remediation.

Acknowledgements

Appendix A. Supplementary data

Supplementary data associated with this article can be found, in the online version, at http://dx.doi.org/10.1016/j.apcatb.2017.10.030.

References

[1] A.A. Ismail, D.W. Bahnemann, Sol. Energy Mater. Sol. Cells 128 (2014) 85–101.
[2] S. Das, W.M.A. Wan Daud, Renew. Sustain. Energy Rev. 39 (2014) 765–805.
[3] E. Casbeer, V.K. Sharma, X.-Z. Li, Sep. Purif. Technol. 87 (2012) 1–14.
[4] H.X. Sang, X.T. Wang, C.C. Fan, F. Wang, Int. J. Hydrogen Energy 37 (2012) 1348–1355.
[5] A. Hamza, I.J. John, B. Mukhtar, J. Mater. Res. Technol. 6 (2017) 1–6.
[6] D. Wu, Y. Jiang, Y. Yuan, J. Wu, K. Jiang, J. Nanopart. Res. 13 (2011) 2875–2886.
[7] Y. Chen, A. Lu, Y. Li, L. Zhang, H.Y. Yip, H. Zhao, P.K. Wong, Environ. Sci. Technol.

45 (2011) 5689–5695.

[8] H. Shi, G. Huang, D. Xia, T.W. Ng, H.Y. Yip, G. Li, T. An, H. Zhao, P.K. Wong, J. Phys. Chem. B 119 (2015) 3104–3111.

[9] Y. Li, A. Lu, S. Jin, C. Wang, J. Hazard. Mater. 170 (2009) 479–486.

[10] Y. Li, A. Lu, C. Wang, X. Wu, Sol. Energy Mater. Sol. Cells 92 (2008) 953–959.

[11] X. Yang, Y. Li, A. Lu, Y. Yan, C. Wang, P.K. Wong, Sol. Energy Mater. Sol. Cells 95 (2011) 1915–1921.

[12] A. Lu, Y. Li, M. Lv, C. Wang, L. Yang, J. Liu, Y. Wang, K.-H. Wong, P.-K. Wong, Sol. Energy Mater. Sol. Cells 91 (2007) 1849–1855.

[13] L.M.S. Colpini, G.G. Lenzi, M.B. Urio, D.M. Kochepka, H.J. Alves, J. Environ. Chem. Eng. 2 (2014) 2365–2371.

[14] A. Simpraditpan, T. Wirunmongkol, S. Pavasupree, W. Pecharapa, Mater. Res. Bull. 48 (2013) 3211–3217.

[15] S.A.K. Leghari, S. Sajjad, F. Chen, J. Zhang, Chem. Eng. J. 166 (2011) 906–915.

[16] D. Xia, Y. Li, G. Huang, C. Fong, T. An, G. Li, H. Yip, H. Zhao, A. Lu, P.K. Wong, Appl. Catal. B: Environ. 176 (2015) 749–756.

[17] D. Xia, Z. Shen, G. Huang, W. Wang, J.C. Yu, P.K. Wong, Environ. Sci. Technol. 49 (2015) 6264–6273.

[18] D. Xia, T. An, G. Li, W. Wang, H.J. Zhao, P.K. Wong, Water Res. 99 (2016) 149–161.

[19] International Organization for Standardization (ISO) 11348-3, Water Quality Determination of the Inhibitory Effect of Water Samples on the Light Eemission of Vibrio fischeri (Luminescent Bacteria Test) Part 3: Method Using Freeze-dried Bacteria, International Organisation for Standardization, Geneva, 2008.

[20] International Organization for Standardization (ISO) 13829, Water Quality Determination of the Genotoxicity of Water and Waste Water Using the Umutest, International Organisation for Standardization, Geneva, 2000.

[21] D. Xia, W. Wang, R. Yin, Z. Jiang, T. An, G. Li, H. Zhao, P.K. Wong, Appl. Catal. B Environ. 214 (2017) 23–33.

[22] D. Xia, T.W. Ng, T. An, G. Li, Y. Li, H.Y. Yip, H. Zhao, A. Lu, P.K. Wong, Environ. Sci.

[23] D. Xia, Y. Li, G. Huang, R. Yin, T. An, G. Li, H. Zhao, A. Lu, P.K. Wong, Water Res. 112 (2017) 236–247.

[24] X.M. Shuai, W.Z. Shen, J. Phys. Chem. C 115 (2011) 6415–6422.

[25] C. Yao, Q. Zeng, G.F. Goya, T. Torres, J. Liu, H. Wu, M. Ge, Y. Zeng, Y. Wang, J.Z. Jiang, J. Phys. Chem. C 111 (2007) 12274–12278.

[26] X. Zhao, M. Li, X. Lou, Mater. Sci. Semicond. Process 16 (2013) 489–494.

[27] X. Wu, K. Li, H. Wang, J. Hazard. Mater. 174 (2010) 573–580.

[28] S.D. Jadhav, P.P. Hankare, R.P. Patil, R. Sasikala, Mater. Lett. 65 (2011) 371–373.

[29] S.E.J. Male, Phys. D: Appl. Phys. 13 (1980) 67–70.

[30] S. Nasrazadani, A. Raman, Corros. Sci. 34 (1993) 1355–1365.

[31] T. Ishikawa, E. Matijevic, Langmuir 4 (1988) 26–31.

[32] K.E. Waters, N.A. Rowson, R.W. Greenwood, A.J. Williams, Sep. Purif. Technol. 56 (2007) 9–17.

[33] D. Xia, T. An, G. Li, W. Wang, H. Zhao, P.K. Wong, Water Res. 99 (2016) 146–161.

[34] D. Xia, I.M.C. Lo, Water Res. 100 (2016) 393–404.

[35] A. Bera, D. Basak, ACS Appl. Mater. Interface 2 (2010) 408–412.

[36] G.V. Buxton, C.L. Greenstock, W.P. Helman, A.B. Ross, W.J. Tsang, Phys. Chem. Ref. Data 17 (1988) 513–886.

[37] M. Ahmad, X. Yan, J.J. Zhu, Phys. Chem. C 115 (2011) 1831–1837.

[38] Q. Xiao, L. Ouyang, Chem. Eng. J. 148 (2009) 248–253.

[39] S. Parvez, C. Venkataraman, S. Mukherji, Environ. Int. 32 (2006) 265–268.

[40] I. Arslan-Alaton, T. Olmez-Hanci, G. Korkmaz, C. Sahin, Chem. Eng. J. 318 (2016) 64–75.

[41] S. Frassinetti, C. Barberio, L. Caltavuturo, F. Fava, D. Di Gioia, Ecotoxicol. Environ. Saf. 74 (2011) 253–258.

[42] UMU-Chromo TestTM, Kit ISO, Version 1.2, Environmental Bio-Detection Products, Inc. (EBPI), Ontario, 2012.